Journal of Magnetic Resonance 303 (2019) 82–90

Contents lists available at ScienceDirect

Journal of Magnetic Resonance

journal homepage: www.elsevier.com/locate/jmr

Electropermanent magnets for variable-field NMR

Chad Ropp [a], Cheng Chen [b], Mason Greer [b], Jarred Glickstein [b], Lamar Mair [a], Olivia Hale [a], David Ariando [b], Sahar Jafari [a], Anjana Hevaganinge [a], Soumyajit Mandal [b,*], Irving N. Weinberg [a]

[a] Weinberg Medical Physics, 12156 Parklawn Dr, Rockville, MD 20852, USA
[b] Case Western Reserve University, 10900 Euclid Ave, Cleveland, OH 44106, USA

ARTICLE INFO

Article history:
Received 8 March 2019
Revised 15 April 2019
Accepted 16 April 2019
Available online 24 April 2019

Keywords:
Variable field NMR
T_1 dispersion
Electropermanent magnet
Broadband

ABSTRACT

In this work, a dynamically tunable B_0 field is used to perform variable-field NMR. The system consists of an array of electropermanent AlNiCo-5 magnets whose magnetizations are individually programmed using pulse-power control. This design allows the field strength to be varied for field-dispersion measurements. An ultra-broadband front-end is utilized that maintains efficient power transmission over a broad range of frequencies for robust operation without probe tuning. We perform $T_1 - T_2$ correlation measurements at various B_0 field strengths (0.5–2 MHz) and demonstrate discrimination of different dairy products. We observe variation in the frequency dependence of the proton spin–lattice relaxation for the different products as a function of the degree of protein hydration. This variable-field technique provides a low-cost alternative to fast field-cycling NMR and could open possibilities for novel contrast measurements and spatial encoding in magnetic resonance imaging.

© 2019 Elsevier Inc. All rights reserved.

1. Introduction

Many of today's NMR technologies require operation at dedicated high magnetic fields. Maintaining these fields can introduce prohibitive costs [1], safety risks [2,3], and portability issues [4]. Versatile NMR platforms whose field can be turned on and off will be important for expanded use in next generation technologies. In addition, systems whose magnetic field can be smoothly varied from one field strength to another could enable new protocols for material characterization using field-dispersion measurements.

Field-dispersion NMR is currently used to analyze sample spoilage [5], material composition [6], and elemental constituents [7]. Current technologies rely on fast field cycling (FFC) systems that introduce a transient perturbation to the dedicated B_0 field. For FFC, creating strong dB/dt perturbations is required in order to manipulate nuclear spins within the T_1 time of the sample, which often limits sample volumes and requires dedicated heat management. Moreover, FFC technologies often employ high B_0 fields for detection and thus require strong field perturbations to map field-dispersive behavior, which often occurs at low field strengths [8]. The fact that dispersion occurs at low fields opens the possibility for utilizing recent advances in low-field NMR [9,10] for performing field-dispersion characterization. These advances improve functionality, portability, and overall system cost [11–13]. Most of these low-field designs use NdFeB or SmCo permanent magnets as they offer sufficient remnant fields and coercivity needed for NMR experiments [13,14]. The use of other permanent magnets, such as AlNiCo, for low-field NMR applications has largely been unexplored.

In this paper we demonstrate a variable-field NMR system capable of performing field-dispersion measurements at low magnetic field strengths. We use the system to study the field-dependent relaxation of various dairy products using 2-D $T_1 - T_2$ correlation measurements. Our variable-field system consists of an array of AlNiCo-5 electropermanent magnets, whose magnetizations are dynamically tuned through pulse-power control. In particular, we were able to smoothly tune our B_0 field from 38 to 14 mT, i.e., by nearly a factor of 3. This variable-B_0 system is combined with a broadband probe and analog front-end (transmitter and receiver) for tracking changes in NMR relaxation rates. We demonstrate that our design is compatible with conventional NMR pulse sequences and can be used to create a variable-field platform that is portable and low-cost.

2. System overview and theory

This paper focuses on variable-field NMR measurements that combine a reconfigurable electropermanent magnet array with a broadband probe and analog front-end. Recent developments in broadband NMR have been used for nuclear quadrupole resonance (NQR) measurements, multi-nuclear experiments, and multi-slice

* Corresponding author.
E-mail addresses: cxc717@case.edu (C. Chen), sxm833@case.edu (S. Mandal).

https://doi.org/10.1016/j.jmr.2019.04.010
1090-7807/© 2019 Elsevier Inc. All rights reserved.

experiments in strong gradients [15–17]. Although their use in NMR is limited [14], AlNiCo-5 magnets have a low coercivity [13], which enables their magnetization to be easily controlled to create a reconfigurable B_0 field. Additionally, AlNiCo-5 magnets have low temperature coefficients [18], which make them robust to temperature changes due to thermal drift and heating during magnetization. A diagram of the operating principle is shown in Fig. 1.

Fig. 1 shows that a fully magnetized magnet is demagnetized to different field strengths along its *B-H* curve through a series of electromagnetic pulses. The resulting decrease in B_0 field strength causes a shift to lower frequencies in the NMR spectrum, which is measured using the broadband spectrometer. A block diagram of the experimental system is shown in Fig. 2 which highlights the broadband front-end and the pulsed electropermanent magnet systems. The spectrometer interfaces with a computer through a benchtop NMR spectrometer (Kea2, Magritek), while the pulse-power system is controlled by the same computer through a MATLAB script.

2.1. Reconfigurable B_0 design

A picture of the working system is shown in Fig. 3. Our B_0 field generation system consists of four electropermanent magnets mounted in a 3D-printed holder. Each magnet is a one-inch diameter, six-inch long rod of AlNiCo-5. AlNiCo-5 has a relatively high remnant magnetic field strength of 1.2 T, but is limited by the aspect ratio of the material [13]. When fully magnetized, the AlNiCo-5 rods we use have a field strength of about 150 mT on axis when measured 1 mm away from their surface. Each magnet is wound 50 times with a 14 AWG wire, creating a solenoid with an inductance of 25 μH. Magnet windings and cables are covered with copper tape and an insulating metal sleeve, respectively, and grounded to reduce noise in the NMR signal.

The magnetization of the AlNiCo magnets are controlled dynamically using a pulse-power system that discharges an array of capacitors using a pulse-width-modulated signal. The capacitor array and channel selector, which diverts the discharge pulse to different magnets, were purchased from Eagle Harbor Technologies (Seattle, WA). The channel selector also controls the polarity of the electromagnetic pulses, which is used to magnetize, demagnetize, and flip the magnetization of the AlNiCo magnets. The waveforms of several typical discharge pulses are shown in Fig. 4. Plotted is the time-dependent current through the solenoid wrapping a single magnet and measured using a transformer probe. For each waveform the capacitors are discharged for 10 ms using an electrical relay, which is pulse-width modulated with a period of 100 μs

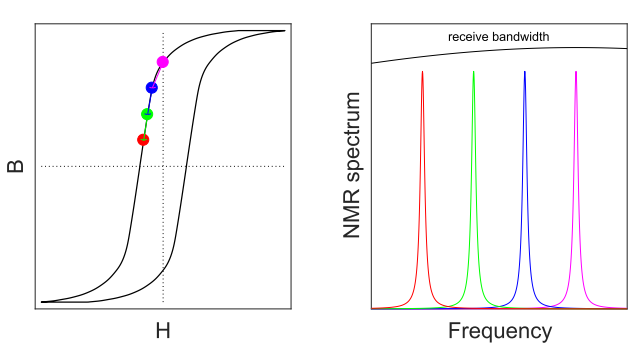

Fig. 1. The working principle for variable-field NMR using sequential demagnetization of an electropermanent magnet. (a) Ideal *B-H* curve for an electropermanent magnet, highlighting points along the degmanetization curve. (b) Demagnetization of B_0 will cause a shift in the Larmor frequency. The shifted NMR spectra all reside within the bandwidth of the broadband receiver.

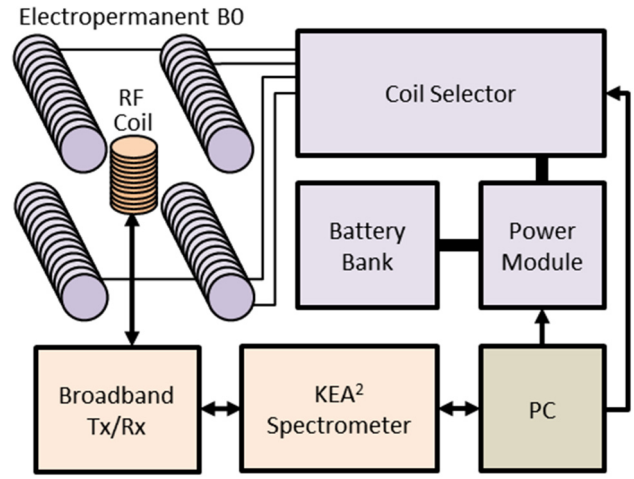

Fig. 2. Block diagram of the variable NMR system.

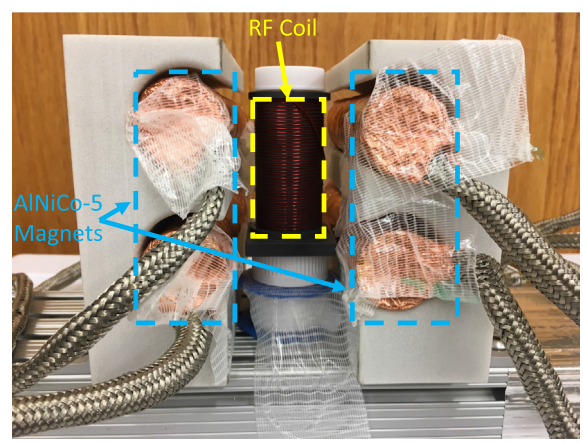

Fig. 3. Image of the NMR setup.

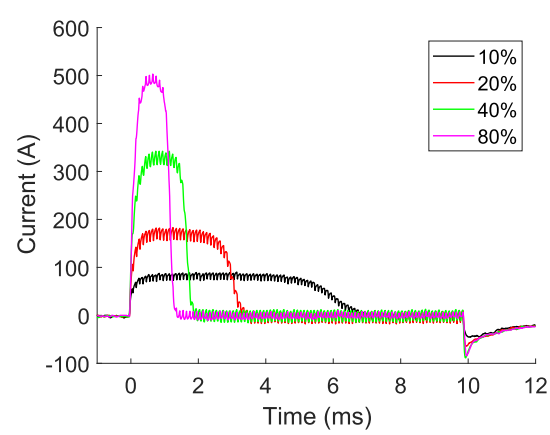

Fig. 4. Measured current through the coil of a wound magnet. The power relay is triggered with different duty cycles to control the discharge of a capacitor array within a 10 ms time window. Longer duty cycles allow the capacitor to discharge faster, reaching higher peak currents.

and different duty cycles (corresponding to different colors). Higher duty cycles discharge the capacitor array faster, creating shorter pulses and a higher current that can be used to more substantially change the magnetization of the AlNiCo magnet. The maximum current is reached using a 90% duty cycle pulse (not shown) that reaches 600 A.

Demagnetization of the AlNiCo magnets can be reproducibly controlled through judicious control of the duty cycle of the discharge pulses. Fig. 5 plots the magnetic field measured 1 mm away from a single AlNiCo magnet as different duty cycle pulses are applied in series to first demagnetize and then flip its magnetization. Several cycles of this procedure are performed with the standard error in the magnetic field strength between cycles shown with error bars. As the duty cycle is increased, the magnet demagnetizes towards zero along a fairly linear trend. As more current is applied with longer duty cycle pulses the magnet begins to remagnetize and saturate in the opposite direction. By operating in the linear regime, each magnet contributing to the B_0 field can be sequentially demagnetized to reduce the B_0 field strength without compromising homogeneity. Plotted in Fig. 6 is the measured NMR spectrum of $CuSO_4$-doped water at decreasing magnetic fields. The field was reduced from 38 to 32, 26, 20, and 14 mT by pulsing each magnet with 0, 2, 4, 6, and 8% duty cycle pulses respectively. The width of the NMR spectrum remains approximately constant as the field homogeneity is maintained through this pulsing sequence.

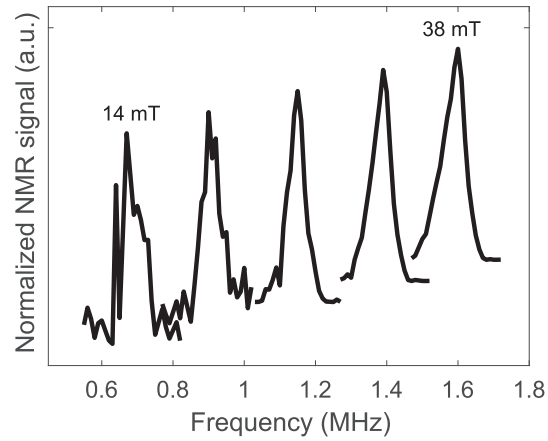

Fig. 6. Measured NMR spectra at different B0 field strengths. The electropermanent magnet array was pulsed using a sequence of 2, 4, 6, 8, and 10% duty cycle pulses causing the peak field to shift between 38, 32, 26, 20, and 14 mT respectively.

2.2. Broadband front-end design

The coil used in the variable-field experiments was made by winding AWG 20 wire around a hollow PVC cylinder as shown in Fig. 3. The solenoid consisted of 38 turns with an effective diameter and length of 32 mm and 60 mm, respectively. It was interfaced to an ultra-broadband front-end based on a design originally published in [15]. This front-end is ideally suited for working with the reconfigurable magnet system. Traditional NMR probes apply a passive tuned impedance-matching network to achieve efficient transmission and low-noise reception around the Larmor frequency $\omega_0 = \gamma B_0$. However, this network is inherently narrowband, with an approximate bandwidth of $2\omega_c/Q$, where $\omega_c \approx \omega_0$ is the resonant frequency and Q is the quality factor of the network. The value of Q is often dominated by that of the coil; therefore it is common for Q to be higher than 100, which makes the bandwidth of the probe much smaller than ω_0. As a result, traditional probes have to be manually re-tuned to handle different Larmor frequencies, which is very time-consuming and not automated.

Our ultra-broadband front-end is designed to address this challenge by not using a tuned network for transmission or reception. The system still applies conventional RF pulses for spin excitation. However, unlike in a tuned probe, the transmitter directly controls the RF voltage across the coil so that the amplitude of B_1 is insensitive to changes in coil Q. Since the circuit is impedance-mismatched, all the current flowing in the coil has to be supplied by the transmitter switches (i.e., there is no current amplification as in a resonant network). As a result, the transmit voltage V_{BB} has to be significantly higher than what is used with a conventional matching network in order to generate the same B_1 field. In particular, the B_1 amplitude is given by [15]

$$B_1 \approx \left(\frac{B_1}{I_1}\right)\frac{(4/\pi)\sin(\pi D)V_{BB}}{\omega_0 L}, \tag{1}$$

where (B_1/I_1) is the coil sensitivity (defined by its geometry), $0 < D < 1$ is the duty cycle of the transmitted waveform, and L is the coil inductance. Eq. (1) shows that $B_1 \propto 1/\omega_0$ for a given transmitter voltage waveform. This is because the coil impedance increases $\propto \omega_0$, thus resulting in less current for a given voltage. As a result, the pulse length required to obtain a given flip angle increases as $T_p \propto \omega_0$.

During the receive phase, the system directly senses the voltage induced in the coil. This makes the received signal amplitude insensitive to coil Q, but also makes receiver and duplexer design more challenging by eliminating the passive signal pre-amplification provided by a conventional matching network. Nevertheless, with proper system design, we can use a standard, highly sensitive solenoid coil as the detector while also i) maintaining low noise figure (NF), and ii) obtaining the advantages of rapid frequency and phase switching over a very broad frequency range.

The gain and output-referred noise of the broadband receiver was characterized with the input shorted. These quantities are used to compute its input-referred noise $v_{n,in}^2$. Over the typical operating frequency range of 0.3–3 MHz, the receiver has an input-referred noise of 0.15–0.165 nV/Hz$^{1/2}$. This corresponds to a noise resistance $v_{n,in}^2/4k_bT$ of 1.4–1.7 Ω at 300 K (where k_b is Boltzmann's constant), as shown in Fig. 7(a). The measured series resistance of the coil R_{coil} is also shown for comparison.

By convention, the input-referred noise of an amplifier has both a voltage component e_n^2 and a current component i_n^2. The latter is mainly due to the amplifier's input bias current, which creates a shot noise power spectrum density (PSD) of $i_n^2 = 2q \times I_B$. This current noise is converted to voltage noise by the impedance present across the amplifier input terminals. Ignoring correlations between e_n^2 and i_n^2 for simplicity, the total input-referred noise then becomes

$$v_{n,in}^2 = e_n^2 + i_n^2 \times |Z_{in}||Z_{coil}|^2 = e_n^2 + i_n^2 \times \left|\frac{Z_{in}Z_{coil}}{Z_{in}+Z_{coil}}\right|^2, \tag{2}$$

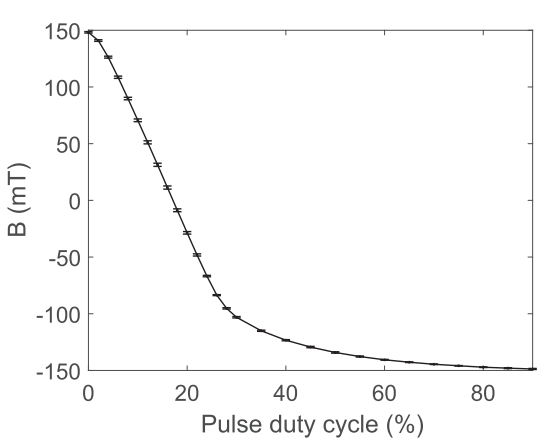

Fig. 5. Measured magnetic field along the axis of a single wound magnet for pulses with different duty cycles. For reducing B_0 we operate in the linear regime between 0–20% duty cycle. Higher duty cycle causes the magnet to flip sign, remagnetize, and ultimately saturate at a negative magnetization.

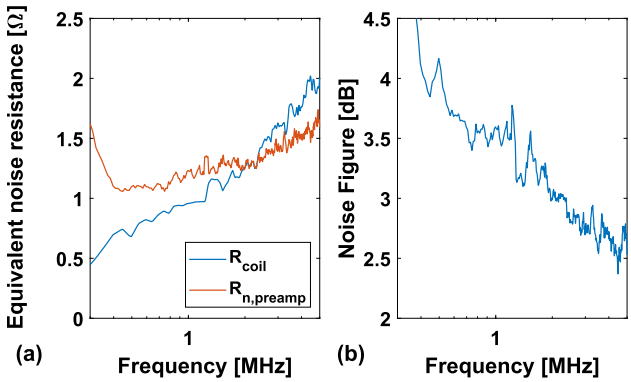

Fig. 7. (a) Measured series resistance of the coil (R_{coil}) and effective input-referred noise resistance of the broadband receiver ($R_{n,preamp}$). (b) Estimated receiver noise figure (NF) based on the data shown in (a).

where "||" means "parallel to". Our broadband receiver uses a low-noise JFET device (BF-862, NXP) to realize the first gain stage, resulting in an extremely low input bias current I_B (approximately 3 pA at room temperature). As a result i_n^2 may be neglected even for high-impedance coils, which makes the amplifier highly effective for use with noise-mismatched loads and results in $v_{n,in}^2 \approx e_n^2$. Thus, the amplifier's input-referred noise is characterized with the input terminals shorted in order to only measure e_n^2.

Noise in the broadband receiver is simply the sum of input-referred noise from the amplifier and thermal noise $4k_bTR_{coil}$ in the coil. The resulting receiver NF is given by

$$NF = \frac{v_{n,in}^2 + 4k_bTR_{coil}}{4k_bTR_{coil}} = 1 + \frac{v_{n,in}^2}{4k_bTR_{coil}}. \quad (3)$$

Fig. 7(b) plots the estimated receiver NF for the chosen sample coil, and confirms that it is acceptable (< 4 dB) for frequencies > 400 kHz.

The detected NMR signal amplitude (assuming inductive detection) increases with Larmor frequency as ω_0^2 [19]. Also, more signals can be acquired per unit time using Carr-Purcell-Meiboom-Gill (CPMG)-like pulse sequences as the echo period T_E decreases, so the precision with which the initial amplitude and decay rate can be estimated also improves. Given these factors, the signal to noise ratio (SNR) of the received signal in root-mean-squared (rms) units can be written as

$$SNR \propto \frac{\omega_0^2(B_1/I_1)V_S}{\sqrt{4k_bTR_{coil} \times NF \times \Delta f}} \times \frac{1}{\sqrt{T_{E,min}}}, \quad (4)$$

where V_S is the sample volume, Δf is the final bandwidth for detecting the signal, and $T_{E,min}$ is the minimum available echo spacing in a CPMG-like pulse sequence. A detailed justification for the $1/\sqrt{T_{E,min}}$ term in this equation can be found in Appendix A. Assuming that i) the coil is skin effect-limited ($R_{coil} \propto \sqrt{\omega}$), and ii) $T_{E,min}$ and the receiver NF are constant (frequency-independent), we get the well-known scaling relationship $SNR \propto \omega_0^{7/4}$.

However, in the broadband system, the pulse length T_p required for a given flip angle increases with ω_0 as predicted by Eq. (1). Moreover, it is reasonable to assume that $T_{E,min} \propto T_{180}$ where T_{180} is the length of the refocusing pulse; this is generally limited by a combination of allowable transmitter duty cycle T_p/T_E and receiver settling time. Thus, $T_{E,min}$ for the broadband front-end decreases at low frequencies, allowing experiments to be performed at lower echo periods T_E and improving SNR as predicted by Eq. (4). In particular, to a good approximation $T_{E,min} \propto \omega_0$, which results in $SNR \propto \omega_0^{5/4}$ for a skin effect-limited coil.

Fig. 8 compares the relative SNR of the broadband system as a function of frequency with and without taking the effects of varying $T_{E,min}$ into account. These plots were generated by using the measured frequency-dependent values of receiver input-referred noise $v_{n,in}^2$ and coil resistance R_{coil} in order to obtain accurate results. The theoretical relationships $SNR \propto \omega_0^{7/4}$ (with $T_{E,min}$ constant) and $SNR \propto \omega_0^{5/4}$ (with $T_{E,min} \propto \omega_0$) are also shown for comparison.

Fig. 8 shows that the broadband front-end can obtain sufficient SNR over a broad frequency range without manual re-tuning, thus allowing us to fully exploit the advantages of a reconfigurable magnet system. Its nominal operating frequency range is 0.3–3 MHz, which covers the entire Larmor frequency range of interest. Furthermore, it allows very rapid switching of the RF frequency to meet the needs of field-dispersion measurements. In addition, the front-end provides features such as programmability, flexibility, and robustness, making its integration with the magnet array simple and straightforward.

3. Results

3.1. Experimental setup and basic measurements

We use an improved version of the ultra-broadband design which physically separates the transmitter and receiver so that the system is smaller in size and easy to operate [16]. During the experiments, both broadband front-end and reconfigurable magnet system were placed inside a Faraday cage to reduce external RF interference.

All selected samples were measured at four different Larmor frequencies (2180 kHz, 1770 kHz, 1070 kHz, and 512 kHz). Absolute phase effects were observed to cause significant long-lived transients in the echo decay curves at the lowest measurement frequency (512 kHz). These effects were eliminated by ensuring that all pulse lengths and time delays in the pulse sequence were integer multiples of the RF period $2\pi/\omega_0$ [20]. For example, the echo period, $\pi/2$ pulses, and π pulses for the 512 kHz experiments were set to 70, 4, and 7 RF periods (136.5, 7.8, and 13.65 μs), respectively.

In order to examine the long-term stability of the AlNiCo-5 magnet array, we performed the same CPMG experiments five months apart on a doped-water sample. The magnets were initially programmed to a Larmor frequency near 512 kHz and not reprogrammed during this period. Fig. 9 compares data from the two sets of experiments. The curves show that the field strength and

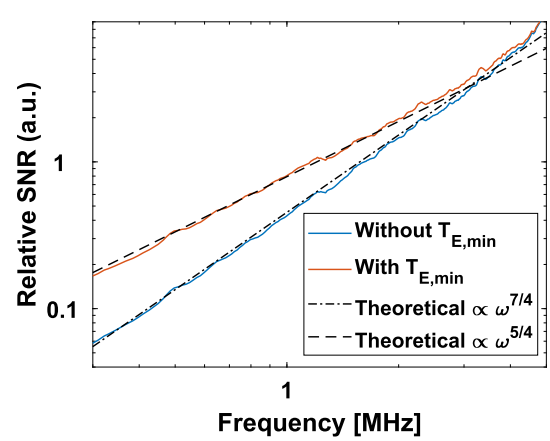

Fig. 8. SNR trend modeled by Eq. (4) using measured values of R_{coil}, $v_{n,in}^2$, and $T_{E,min}$. The theoretical relationships $SNR \propto \omega_0^7/4$ and $SNR \propto \omega_0^5/4$ expected for a skin effect-limited coil are also shown. for comparison.

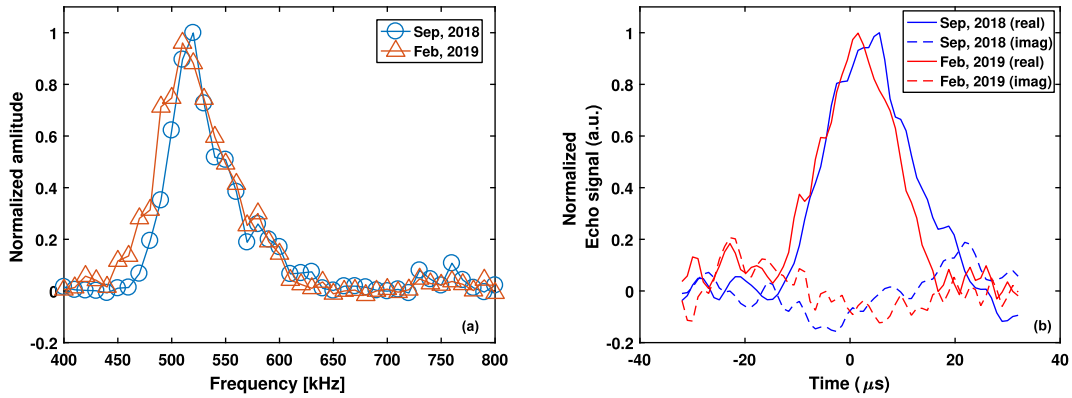

Fig. 9. Comparison between the same CPMG experiments performed on a doped-water sample five months apart. There is no obvious magnetic field decay.

inhomogeneity show no significant change. This result proves that our AlNiCo-5 magnet array has strong field retention power, thus allowing it to offer both the advantages of a permanent magnet (stable static field) and an electromagnet (programmable field).

3.2. Characterization of dairy products

We study the advantages of our setup by performing $T_1 - T_2$ correlation measurements at different B_0 field strengths and demonstrating the difference in this correlation for various dairy products. The physical state of water in a food system has an important influence on both its structural and functional properties. As a popular technique for ^{1}H analysis, NMR has proven to be powerful for assessing difference in the structure and component mobility of foods. In particular, NMR is able to provide a great deal of information on the properties of casein solutions such as milk [21] and cheese with different degree of hydration [5]. Moreover, earlier work has demonstrated that different dairy products can be distinguished by their T_1 dispersion curves [5]. The shapes of these curves depend on differences between molecular motion in bulk solution and in the vicinity of a source of relaxation, such as proteins. Thus, field-dispersion NMR provides information on the motion of water molecules and their interaction with proteins, which are known to be correlated with cheese ripening mechanisms. The ultra-broadband feature of our setup provides feasibility to deliver the results of field-dispersion NMR without any hardware modification, which makes it ideal to analyze this type of experiments.

All food products tested were purchased at a local grocery store. The samples with different protein concentration were carefully selected in order to show different dispersion curves versus the B_0 field. Table 1 shows the samples tested and the quantity of protein contained in the standard quantity (1 oz) or volume (1 cup) listed on each sample product. Water doped with $CuSO_4$ (4% concentration) was also measured as a reference. Samples were prepared in standard NMR tubes which can be fit tightly into the coil holder as seen in Fig. 3. They were stored in a refrigerator and only taken out during experiments in order to maintain freshness. Moreover, all experiments were finished within four days to ensure that all samples were still within their expiration dates.

We utilize a standard inversion recovery (IR) pulse sequence with CPMG-based signal acquisition for $T_1 - T_2$ measurements. The IR-CPMG sequence is shown in Fig. 10. The CPMG condition requires the phases of the excitation and refocusing pulses in the rotating frame to be separated by $\pi/2$; we denote these by $(\pi/2)_x$ and π_y respectively. Moreover, an extra π_y pulse before CPMG pulse sequence is required for IR. A 4-part phase cycle is used for the IR-CPMG sequence. T_1 information can be extracted from the IR period by using different τ values, while T_2 information is collected during the CPMG period. Experiments were repeated three times to increase the SNR. Given the averaged time-domain data, we used a regularized 2-D fast Laplace inversion (FLI) algorithm [22] to generate $T_1 - T_2$ distribution functions $f(T_1, T_2)$. The optimum value of the FLI regularization parameter depends on measurement SNR and was selected using a version of the well-known Butler-Reeds-Dawson algorithm [23].

The resulting $T_1 - T_2$ distributions were plotted and analyzed. The full set of results are presented in Appendix B; here we summarize our main findings. For the bulk liquids, i.e., doped water, milk, and Soylent (a liquid marketed as a meal replacement, referred to as "soy protein drink" in the following sections), both T_1 and T_2 distributions were found to remain almost constant versus Larmor frequency. On the contrary, the T_1 distributions of cheese were found to change significantly. In order to quantify these observations, we directly estimated the logarithmic means of T_1 and T_2 from 1-D projections of the measured 2-D $T_1 - T_2$ distribution functions. Fig. 11 summarizes the resulting relaxation dispersion curves (log means of $1/T_1$ and $1/T_2$ distributions versus frequency) on a log scale. These plots confirm significant T_1 dispersion for the cheese samples, while there is negligible T_2 dispersion for all liquid samples as expected [24].

The measured dispersion curves are in agreement with [5]. Cheese products generally consist of fat globules and water aggre-

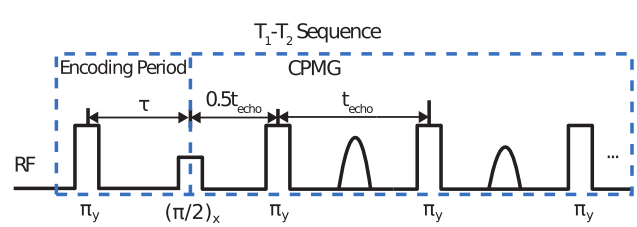

Fig. 10. The pulse sequence used for 2-D $T_1 - T_2$ correlation experiments. The delay τ is stepped over multiple experiments to extract the T_1 data.

Table 1
Estimated protein content for the measured samples based on information in the product labels.

Sample	Milk	Soy protein drink	Parmesan	Cheddar	Mozzarella
Sample quantity	240 ml	240 ml	28 g	28 g	28 g
Protein quantity	8 g	11.6 g	10 g	7 g	5 g

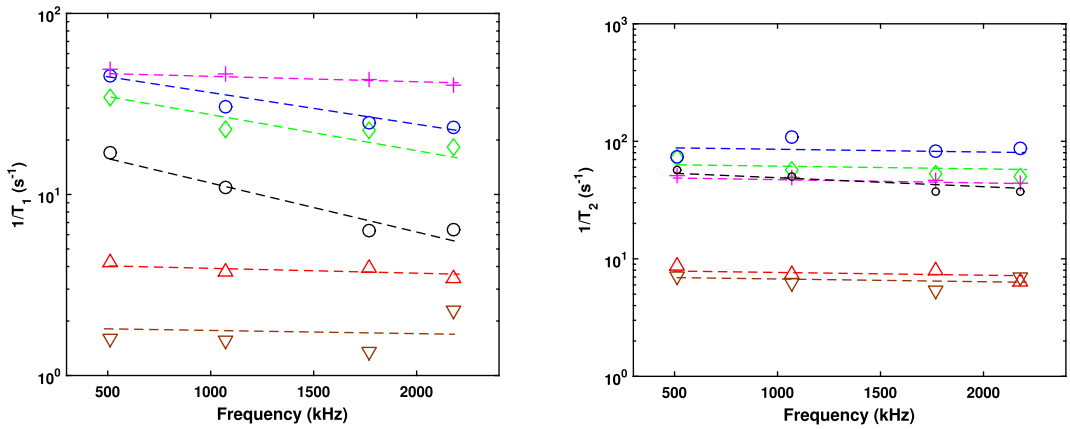

Fig. 11. Measured proton NMR dispersion curves for soy protein drink (red), cheddar cheese (green), parmesan cheese (blue), mozzarella cheese (black), milk (brown), and water (purple). The spin-lattice relaxation rates ($1/T_1$) of liquids don't have an obvious change while those of cheese products decrease with frequency. The dacay rate is lower with the degree of protein hydration increases. In addition, the spin–spin relaxation rates ($1/T_2$) of the samples don't have an obvious change. (For interpretation of the references to colour in this figure legend, the reader is referred to the web version of this article.)

gations. Nuclear spin-lattice relaxation in the water/protein systems can be considered as arising from two spin populations coupled by chemical exchange. A single relaxation rate is assigned to each population as mixing occurs, by fast spin diffusion in the case of the solid (protein protons) and by fast chemical exchange and molecular translation for the liquid (water) [25]. The change in relaxation rate across frequency will be smaller for hydrated cheese compared to dry cheese. This is due to coupling between the water proton and the rotationally immobilized protons in the protein embedded in the cheese. The observed relaxation features suggest that the theory is applicable to water hydration of proteins.

4. Summary and conclusions

A programmable B_0 system has been proposed for performing variable-field NMR. The system relies on electrically-reconfigurable magnet arrays that are (i) easy to program, (ii) robust and capable of being dynamically reprogrammed, and (iii) consume no static power after tuning (unlike electromagnets). These properties enable a flexible, portable, and low-cost system for variable-field NMR experiments. Furthermore, the use of an ultra-broadband analog front-end enables the system to use conventional pulse sequences and transmit/receive coils over the entire operating frequency range without manual re-tuning. The ability to adjust or even sweep the B_0 field makes this system attractive for magnetic resonance applications such as imaging of living organisms, food and materials examination, and potentially dynamic nuclear polarization (DNP). System functionality is demonstrated by performing $T_1 - T_2$ correlation measurements on dairy products and using the results to distinguish between different products and their rates of spoilage.

Acknowledgements

The authors would like to acknowledge the National Science Foundation (NSF) for funding support. This work was partially funded by the NSF through grant CCF-1563688.

Appendix A. Estimation of Effective SNR for CPMG-like Measurements

We would like to analyze the precision of a CPMG-like multi-echo pulse sequence (e.g., the IR-CPMG pulse sequence used in this paper) when we sum up N_E of the received echoes to maximize the SNR for T_1 measurements. The echo period is defined as T_E. Also, the observed noisy echo decay curve is assumed to be mono-exponential for simplicity, i.e., is modeled by $r(k) = s(0)e^{-kT_E/T_2} + n$ where the first term is the signal, and the second is additive white Gaussian noise.

Without additional matched filtering, the noisy received signal obtained by adding up N_E echoes is given by

$$r_{tot} = \sum_{k=1}^{N_E} \left[s(0)e^{-kT_E/T_2} + n \right]. \tag{A.1}$$

Considering the signal term separately, we get

$$s_{tot} = s(0) \sum_{k=1}^{N_E} e^{-kT_E/T_2} = s(0) \frac{1 - e^{-N_E T_E/T_2}}{1 - e^{-T_E/T_2}}. \tag{A.2}$$

In most cases it is safe to assume that $T_E \ll T_2$. In this case $1 - e^{-T_E/T_2} \approx 1 - 1 + T_E/T_2 = T_E/T_2$, so we get

$$s_{tot} = s(0) \left(\frac{T_2}{T_E} \right) \left(1 - e^{-N_E T_E/T_2} \right). \tag{A.3}$$

Since the noise terms in each echo are uncorrelated, the total noise term is simply $n_{tot} = n \times \sqrt{N_E}$. Thus, the SNR of the echo sum (in power units) is given by

$$\begin{aligned} SNR_{tot} &= \frac{s_{tot}^2}{n_{tot}^2} = \frac{s^2(0)}{n^2} \left(\frac{T_2}{T_E} \right)^2 \frac{\left(1 - e^{-N_E T_E/T_2}\right)^2}{N_E} \\ &= \frac{s^2(0)}{n^2} \left(\frac{T_2}{T_E} \right) \frac{\left(1 - e^{-N_E T_E/T_2}\right)^2}{(N_E T_E/T_2)}. \end{aligned} \tag{A.4}$$

It can be shown that matched filtering provides the optimum SNR in the presence of additive white noise. The principle of matched filtering in this case is to weigh each received echo by its expected SNR before summation. For the k-th echo, the weighting factor is e^{-kT_E/T_2} since the signal decays exponentially while the noise remains constant. The value of T_2 may be found iteratively if it is not known *a priori*, as described in [26].

In this case, the noisy received signal (weighted sum of echoes) is given by

$$r_{tot} = \sum_{k=1}^{N_E} \left[s(0)e^{-kT_E/T_2} + n \right] e^{-kT_E/T_2}. \tag{A.5}$$

Considering the signal term separately, we get

$$s_{tot} = s(0) \sum_{k=1}^{N_E} e^{-2kT_E/T_2} = s(0) \frac{1 - e^{-2N_E T_E/T_2}}{1 - e^{-2T_E/T_2}}. \tag{A.6}$$

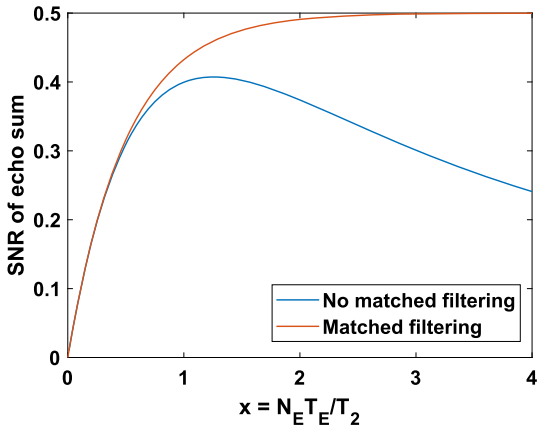

Fig. A.12. Estimated SNR of the echo sum (in power units) for CPMG-like experiments with and without the use of matched filtering along the decay dimension.

Again assuming $T_E \ll T_2$, we have $1 - e^{-2T_E/T_2} \approx 1 - 1 + 2T_E/T_2 = 2T_E/T_2$, so

$$s_{tot} = s(0)\left(\frac{T_2}{2T_E}\right)\left(1 - e^{-2N_E T_E/T_2}\right). \tag{A.7}$$

The noise term is now given by

$$n_{tot} = n \times \sqrt{\sum_{k=1}^{N_E} e^{-2kT_E/T_2}} = n\sqrt{\frac{1-e^{-2N_E T_E/T_2}}{1-e^{-2T_E/T_2}}} \approx n\sqrt{\left(\frac{T_2}{2T_E}\right)\left(1 - e^{-2N_E T_E/T_2}\right)}. \tag{A.8}$$

Thus, the SNR of the weighted echo sum (in power units) is given by

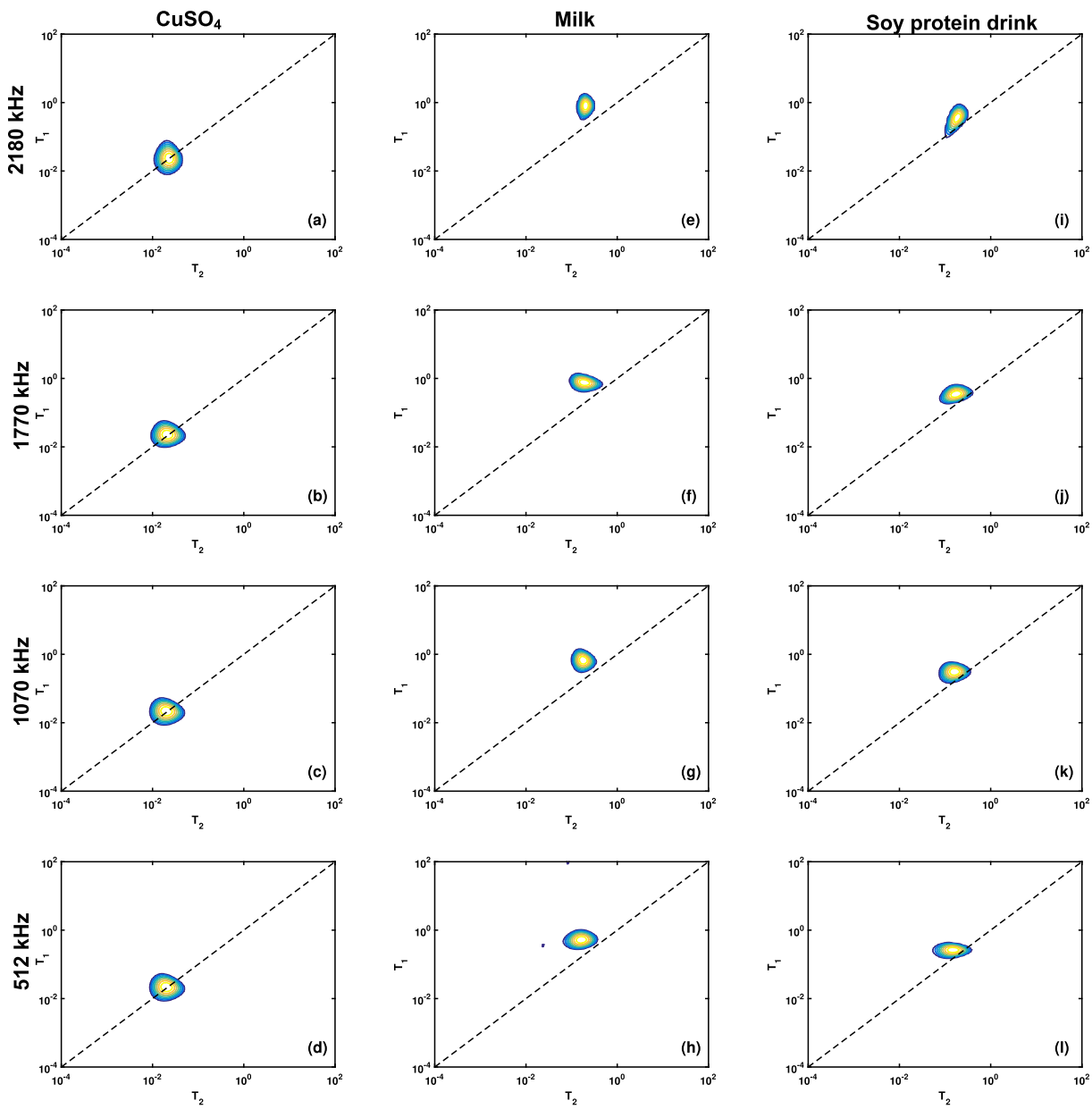

Fig. B.13. Measured $T_1 - T_2$ correlation functions of (a–d) $CuSO_4$ solution, (e–g) milk, and (i–l) soy protein drink samples at different frequencies.

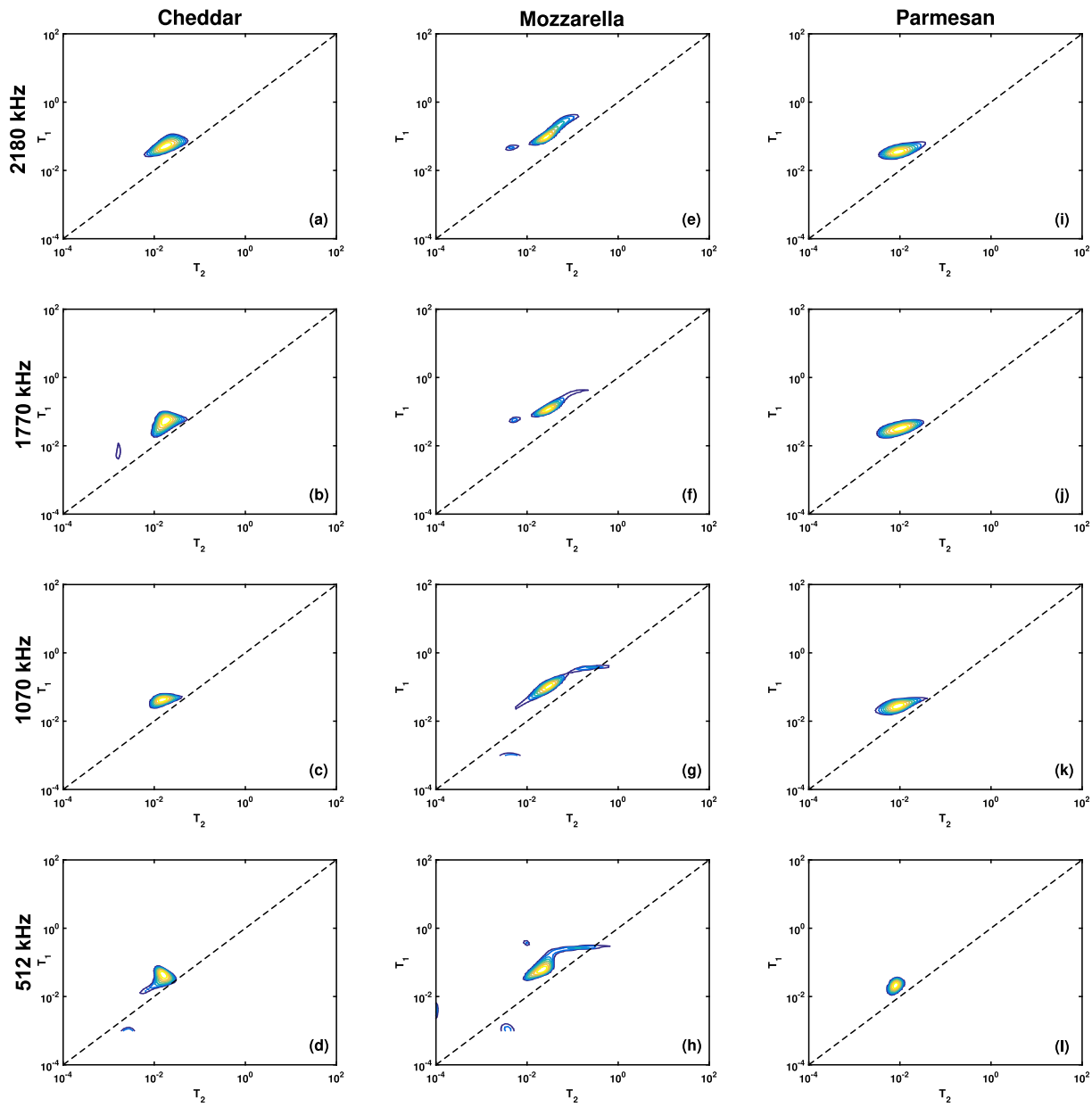

Fig. B.14. Measured $T_1 - T_2$ correlation functions of (a–d) cheddar, (e–g) mozzarella, and (i–l) parmesan cheese samples at different frequencies. Each sample has obvious change with frequency decreases.

$$SNR_{tot} = \frac{s_{tot}^2}{n_{tot}^2} = \frac{s^2(0)}{n^2}\left(\frac{T_2}{2T_E}\right)\left(1 - e^{-2N_E T_E/T_2}\right). \tag{A.9}$$

Let us define the dimensionless variable $x = N_E T_E / T_2$, which represents the normalized duration of the scan (in T_2 units). The two expressions for SNR defined by Eqs. (A.4) and (A.9) then become

$$\begin{aligned} SNR_{tot} &= \frac{s^2(0)}{n^2}\left(\frac{T_2}{T_E}\right)\frac{(1-e^{-x})^2}{x} \quad \text{and} \\ SNR_{tot} &= \frac{s^2(0)}{n^2}\left(\frac{T_2}{T_E}\right)\frac{(1-e^{-2x})}{2}. \end{aligned} \tag{A.10}$$

These two SNR expressions are plotted in Fig. A.12. The figure shows that as x increases, matched filtering (i.e., taking the estimated T_2 decay into account) provides significantly better SNR than simply summing up the noisy echoes. This is because the signal decays exponentially with x while the noise remains constant, which causes the SNR per echo to decrease. However, in either case the SNR scales as $1/T_E$ in power units, which explains the $1/\sqrt{T_{E,min}}$ term in Eq. (4). Note that similar conclusions also hold for more general multi-exponential decay curves.

Appendix B. Complete summary of test samples' $T_1 - T_2$ distributions

In this section, the complete $T_1 - T_2$ distributions of the test samples are presented for reference. Fig. B.13 shows the measured $T_1 - T_2$ distributions for bulk liquids, i.e. doped water, milk, and Soylent (a liquid marketed as a meal replacement, referred to as "soy protein drink" in the paper). Similarly, Fig. B.14 shows the measured distributions for the cheese samples. Note that we did not choose optimum values for the regularization parameter α while generating Figs. B.13 and B.14. Instead, we chose a larger value of α in order to obtain smooth solutions that visually highlight any trends versus Larmor frequency. However, the

optimally-regularized solutions were used to create the dispersion curves shown in Fig. 11.

References

[1] J. Fletcher, M.D. Clark, F.A. Sutton, R. Wellings, K. Garas, The cost of MRI: changes in costs 1989–1996, Brit. J. Radiol. 72 (857) (1999) 432–437, https://doi.org/10.1259/bjr.72.857.10505004, pMID: 10505004.

[2] J. Marshall, T. Martin, J. Downie, K. Malisza, A comprehensive analysis of MRI research risks: in support of full disclosure, Can. J. Neurol. Sci./J. Can. Sci. Neurol. 34 (1) (2007) 11–17, https://doi.org/10.1017/S0317167100005734.

[3] M.J.P. van Osch, A.G. Webb, Safety of ultra-high field MRI: what are the specific risks?, Curr Radiol. Rep. 2 (8) (2014) 61, https://doi.org/10.1007/s40134-014-0061-0.

[4] Y. Lvovsky, P. Jarvis, Superconducting systems for MRI-present solutions and new trends, IEEE Trans. Appl. Supercond. 15 (2) (2005) 1317–1325, https://doi.org/10.1109/TASC.2005.849580.

[5] S. Godefroy, J.-P. Korb, L.K. Creamer, P.J. Watkinson, P.T. Callaghan, Probing protein hydration and aging of food materials by the magnetic field dependence of proton spin-lattice relaxation times, J. Colloid Interf. Sci. 267 (2) (2003) 337–342.

[6] R. Kimmich, R.-O. Seitter, U. Beginn, M. Möller, N. Fatkullin, Field-cycling NMR relaxometry of polymers confined to artificial tubes: verification of the exponent 3/4 in the spin–lattice relaxation dispersion predicted by the reptation model, Chem. Phys. Lett. 307 (3) (1999) 147–152, https://doi.org/10.1016/S0009-2614(99)00505-9, <http://www.sciencedirect.com/science/article/pii/S0009261499005059>.

[7] A.F. Privalov, S.V. Dvinskikh, F. Fujara, H.M. Vieth, Frequency-dependent spin-lattice relaxation study of transport processes in superionic conductors, Appl. Magn. Reson. 15 (3) (1998) 353–361, https://doi.org/10.1007/BF03162021.

[8] E. Anoardo, G. Galli, G. Ferrante, Fast-field-cycling NMR: applications and instrumentation, Appl. Magn. Reson. 20 (3) (2001) 365–404, https://doi.org/10.1007/BF03162287.

[9] B. Blümich, K. Singh, Desktop NMR and its applications from materials science to organic chemistry, Angew. Chem. Int. Ed. 57 (24) (2018) 6996–7010, https://doi.org/10.1002/anie.201707084, <https://onlinelibrary.wiley.com/doi/pdf/10.1002/anie.201707084>.

[10] S.S. Zalesskiy, E. Danieli, B. Blümich, V.P. Ananikov, Miniaturization of NMR systems: desktop spectrometers, microcoil spectroscopy, and "NMR on a chip" for chemistry, biochemistry, and industry, Chem. Rev. 114 (11) (2014) 5641–5694, https://doi.org/10.1021/cr400063g, pMID: 24779750.

[11] H. Raich, P. Blümler, Design and construction of a dipolar halbach array with a homogeneous field from identical bar magnets: NMR mandhalas, Conc. Magn. Reson. Part B: Magn. Reson. Eng. 23 (1) (2004) 16–25, https://doi.org/10.1002/cmr.b.20018, cited By 152.

[12] A. McDowell, E. Fukushima, Ultracompact NMR: 1H spectroscopy in a subkilogram magnet, Appl. Magn. Reson. 35 (1) (2008) 185–195, https://doi.org/10.1007/s00723-008-0151-3.

[13] V. Demas, P.J. Prado, Compact magnets for magnetic resonance, Conc. Magn. Reson. Part A 34 (1) (2009) 48–59, https://doi.org/10.1002/cmr.a.20131, <https://onlinelibrary.wiley.com/doi/pdf/10.1002/cmr.a.20131>.

[14] C. Hugon, P.M. Aguiar, G. Aubert, D. Sakellariou, Design, fabrication and evaluation of a low-cost homogeneous portable permanent magnet for NMR and MRI, Compt. Rend. Chim. 13 (4) (2010) 388–393, https://doi.org/10.1016/j.crci.2009.09.009, <http://www.sciencedirect.com/science/article/pii/S1631074809001581>.

[15] S. Mandal, S. Utsuzawa, D. Cory, M. Hürlimann, M. Poitzsch, Y.-Q. Song, An ultra-broadband low-frequency magnetic resonance system, J. Magn. Reson. 242 (2014) 113–125.

[16] J. Glickstein, S. Mandal, An automated instrument for polarization-enhanced broadband nuclear quadrupole resonance (NQR) spectroscopy, Rev. Sci. Instrum. 89 (9) (2018), 093106.

[17] M. Grisi, G. Gualco, G. Boero, A broadband single-chip transceiver for multi-nuclear nmr probes, Rev. Sci. Instrum. 86 (4) (2015) 044703, https://doi.org/10.1063/1.4916206.

[18] S. Trout, Material selection of permanent magnets, considering thermal properties correctly, in: Proceedings: Electrical Insulation Conference and Electrical Manufacturing and Coil Winding Conference (Cat. No. 01CH37264), IEEE, 2001, pp. 365–370.

[19] D.I. Hoult, R. Richards, The signal-to-noise ratio of the nuclear magnetic resonance experiment, J. Magn. Reson. (1969) 24 (1) (1976) 71–85.

[20] S. Mandal, S. Oh, M.D. Hürlimann, Absolute phase effects on cpmg-type pulse sequences, J. Magn. Reson. 261 (2015) 121–132.

[21] M. Greer, C. Chen, S. Mandal, Automated classification of food products using 2D low-field NMR, J. Magn. Reson. 294 (2018) 44–58.

[22] Y.-Q. Song, L. Venkataramanan, M. Hürlimann, M. Flaum, P. Frulla, C. Straley, T1–T2 correlation spectra obtained using a fast two-dimensional laplace inversion, J. Magn. Reson. 154 (2) (2002) 261–268.

[23] J. Butler, J. Reeds, S. Dawson, Estimating solutions of first kind integral equations with nonnegative constraints and optimal smoothing, SIAM J. Numer. Anal. 18 (3) (1981) 381–397.

[24] J.J. Chen, M. Hürlimann, J. Paulsen, D. Freed, S. Mandal, Y.-Q. Song, Dispersion of T1 and T2 nuclear magnetic resonance relaxation in crude oils, ChemPhysChem 15 (13) (2014) 2676–2681.

[25] R. Bryant, W. Shirley, Dynamical deductions from nuclear magnetic resonance relaxation measurements at the water-protein interface, Biophys. J. 32 (1) (1980) 3–16.

[26] C. Chen, F. Zhang, S. Bhunia, S. Mandal, Broadband quantitative NQR for authentication of vitamins and dietary supplements, J. Magn. Reson. 278 (2017) 67–79.